Received 21 March; accepted 28 November 2005.

1. Lu, Z. H., Lockwood, D. J. & Baribeau, J. M. Quantum confinement and light-emission in SiO_2/Si superlattices. *Nature* **378**, 258–260 (1995).
2. Legrand, B., Agache, V., Nys, J. P., Senez, V. & Stievenard, D. Formation of silicon islands on a silicon on insulator substrate upon thermal annealing. *Appl. Phys. Lett.* **76**, 3271–3273 (2000).
3. Liu, W. & Asheghi, M. Phonon-boundary scattering in ultrathin single-crystal silicon layers. *Appl. Phys. Lett.* **84**, 3819–3821 (2004).
4. Liu, F., Huang, M. H., Rugheimer, P. P., Savage, D. E. & Lagally, M. G. Nanoribbon resistors and the nanomechanical response of a thin silicon film on an insulator. *Phys. Rev. Lett.* **89**, 136101 (2002).
5. Celler, G. K. & Cristoloveanu, S. Frontiers of silicon-on-insulator. *J. Appl. Phys.* **93**, 4955–4978 (2003).
6. Kim, Y. A 0.25 mm 600MHz 1.5V SOI 64b ALPHATM microprocessor. *ISSCC Dig. Tech. Pap. I*, 432–433 (1999).
7. Yan, R. H., Ourmazd, A. & Lee, K. F. Scaling the Si MOSFET — From bulk to SOI to bulk. *IEEE. Trans. Electron. Dev.* **39**, 1704–1710 (1992).
8. Sutter, P., Ernst, W. & Sutter, E. Scanning tunneling microscopy on ultrathin silicon on insulator (100). *Appl. Phys. Lett.* **85**, 3148–3150 (2004).
9. Lin, K. C., Holland, O. W., Feldman, L. C. & Weitering, H. H. Surface characterization of silicon on insulator material. *Appl. Phys. Lett.* **72**, 2313–2315 (1998).
10. Howel, H. *et al.* Status of 300 mm SOI material; comparisons with 200 mm. *Proc. Electrochem. Soc.* **2003-05**, 75–80 (2003).
11. Swartzentruber, B. S., Kitamura, N., Lagally, M. G. & Webb, M. B. Behavior of steps on Si(001) as a function of vicinality. *Phys. Rev. B* **47**, 13432–13441 (1993).
12. Tromp, R. M., Hamers, R. J. & Demuth, J. E. Si(001) dimer structure observed with scanning tunneling microscopy. *Phys. Rev. Lett.* **55**, 1303–1306 (1985).
13. Fortes, E., Patel, J. R. & Comin, F. Direct measurement of the asymmetric dimer buckling of Ge on Si(001). *Phys. Rev. Lett.* **70**, 2790–2793 (1993).
14. Schroder, D. K. *Semiconductor Material and Device Characterization* (Wiley & Sons, New York, 1998).
15. McWhorter, P. J. & Winokur, P. S. Simple technique for separating the effects of interface traps and trapped-oxide charge in metal-oxide-semiconductor transistors. *Appl. Phys. Lett.* **48**, 133–135 (1986).
16. Cristoloveanu, S. & Sheng, L. *Electrical Characterization of Silicon-on-Insulator Materials and Devices* (Kluwer, Boston, 1995).
17. Northrup, J. E. Electronic structure of Si(100)C(4x2) calculated within the GW approximation. *Phys. Rev. B* **47**, 10032–10035 (1993).
18. Stroscio, J. A. & Ho, W. Long-range quasielastic scattering of low-energy electrons by conduction-band surface-plasmons on Si(111)7x7. *Phys. Rev. Lett.* **54**, 1573–1576 (1985).
19. Heike, S., Watanabe, S., Wada, Y. & Hashizume, T. Electron conduction through surface states of the Si(111)-(7x7) surface. *Phys. Rev. Lett.* **81**, 890–893 (1998).
20. Tanikawa, T., Matsuda, I., Kanagawa, T. & Hasegawa, S. Surface-state electrical conductivity at a metal-insulator transition on silicon. *Phys. Rev. Lett.* **93**, 016801 (2004).
21. Petersen, C. L., Grey, F., Shiraki, I. & Hasegawa, S. Micro-four-point probe for studying electronic transport through surface states. *Appl. Phys. Lett.* **77**, 3782–3784 (2000).
22. Yoo, K. & Weitering, H. H. Electrical conductance of reconstructed silicon surfaces. *Phys. Rev. B* **65**, 115424 (2002).
23. Chen, D. X. & Boland, J. J. Chemisorption-induced disruption of surface electronic structure: Hydrogen adsorption on the Si(100)-2x1 surface. *Phys. Rev. B* **65**, 165336 (2002).
24. Chen, D. X. & Boland, J. J. Spontaneous roughening of low-coverage Si(100)-2x1: Cl surfaces: Patch formation on submonolayer halogenated surface. *Phys. Rev. B* **70**, 205432 (2004).
25. Hollinger, G. & Himpsel, F. J. Oxygen chemisorption and oxide formation on Si(111) and Si(100) surfaces. *J. Vac. Sci. Technol. A* **1**, 640–645 (1983).
26. Hamers, R. J. *et al.* Cycloaddition chemistry of organic molecules with semiconductor surfaces. *Acc. Chem. Res.* **33**, 617–624 (2000).
27. Seino, K., Schmidt, W. G. & Bechstedt, F. Organic modification of surface electronic properties: A first-principles study of uracil on Si(001). *Phys. Rev. B* **69**, 245309 (2004).
28. Meuris, M. *et al.* The IMEC clean — A new concept for particle and metal removal on Si surfaces. *Solid State Technol.* **38**, 109–114 (1995).

Supplementary Information is linked to the online version of the paper at www.nature.com/nature.

Acknowledgements This research was supported by the US National Science Foundation, the US Department of Energy, and the US Air Force Office of Scientific Research.

Author Information Reprints and permissions information is available at npg.nature.com/reprintsandpermissions. The authors declare no competing financial interests. Correspondence and requests for materials should be addressed to M.G.L. (lagally@engr.wisc.edu).

LETTERS

Initial corrosion observed on the atomic scale

F. U. Renner[1,2], A. Stierle[1], H. Dosch[1], D. M. Kolb[3], T.-L. Lee[2] & J. Zegenhagen[2]

Corrosion destroys more than three per cent of the world's GDP[1]. Recently, the electrochemical decomposition of metal alloys has been more productively harnessed to produce porous materials with diverse technological potential[2,3]. High-resolution insight into structure formation during electrocorrosion is a prerequisite for an atomistic understanding and control of such electrochemical surface processes. Here we report atomic-scale observations of the initial stages of corrosion of a $Cu_3Au(111)$ single crystal alloy within a sulphuric acid solution. We monitor, by *in situ* X-ray diffraction with picometre-scale resolution, the structure and chemical composition of the electrolyte/alloy interface as the material decomposes. We reveal the microscopic structural changes associated with a general passivation phenomenon of which the origin has been hitherto unclear. We observe the formation of a gold-enriched single-crystal layer that is two to three monolayers thick, and has an unexpected inverted (CBA-) stacking sequence. At higher potentials, we find that this protective passivation layer dewets and pure gold islands are formed; such structures form the templates for the growth of nanoporous metals[3]. Our experiments are carried out on a model single-crystal system. However, the insights should equally apply within a crystalline grain of an associated polycrystalline electrode fabricated from many other alloys exhibiting a large difference in the standard potential of their constituents[4], such as stainless steel (see ref. 5 for example) or alloys used for marine applications, such as CuZn or CuAl.

A common macroscopic fingerprint of the various electrochemical processes that occur during corrosion is provided by so-called cyclic voltammograms (current–voltage curves). Such a cyclic voltammogram for a pristine $Cu_3Au(111)$ surface is shown in Fig. 1a, which is typical for the corrosion behaviour of alloys consisting of components with different noble character[6–8]. A general observation is that—for the initial cycle (performed on the pristine sample)—the current exhibits a pronounced maximum, here in the potential regime between 100 mV and 300 mV (Cu dissolution starts at about 100 mV), which is not observed in subsequent cycles of the voltammogram. This phenomenon has given rise to many speculations about the possible formation of an ultrathin passivation layer. Recent *in situ* electrochemical scanning tunnelling microscopy experiments in this potential regime of passivation revealed the formation of mono-atomic deep vacancies, which have been interpreted as initial dissolution of the more reactive element from Ag-Au (ref. 9) and Cu-Au (refs 10–12) alloy surfaces. Thickness and composition of the passivation layer have been inferred only indirectly from the voltammograms[13].

Above a critical potential E_c the current increases sharply owing to a bulk de-alloying process that produces nanoporous layers of the nobler component. Such a de-alloying process has been observed for binary alloys like Cu-Pd (ref. 14), Ag-Au (refs 2, 15, 16) and Cu-Au (ref. 16). *Ex situ* transmission electron microscopy studies of Cu-Au, Cu-Zn and Ag-Au alloys show evidence for the presence of either pits or three-dimensional islands with a typical size of 5–10 nm (refs 16–19). For controlled production of technically relevant 'corrosion' products like nanoporous materials or related etching patterns, an understanding of the relevant parameters for the formation of patterns with regular morphology below and above the critical potential E_c is necessary. A detailed knowledge of the

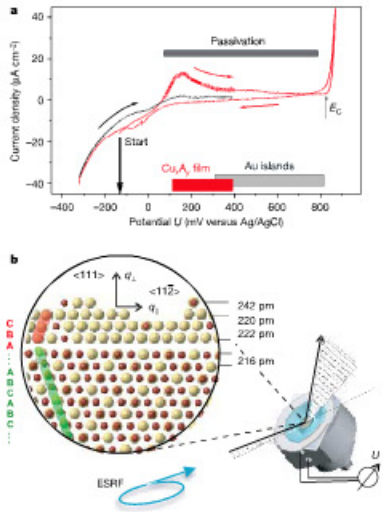

Figure 1 | Voltammogram and passivation layer formation. **a**, Voltammograms recorded at 5 mV s^{-1} show the typical behaviour for corrosion passivation: the red line indicates the virgin current–voltage curve, exhibiting a pronounced maximum between 100 and 300 mV, which is not present in the subsequent cycle (black curve). The bold red curve marks the potential regime in which the X-ray measurements have been performed. Before the passivation breakdown at E_c a current plateau is observed. **b**, Structural model of the ultrathin passivation layer resulting from the fit to the X-ray diffraction data. Au atoms are represented by yellow spheres, and Cu atoms by red spheres. The ABC stacking of the substrate is inverted in the single crystalline overlayer. The two topmost layers are only partially occupied. A schematic view of the *in situ* X-ray diffraction cell is included.

[1]Max-Planck-Institut für Metallforschung, Heisenbergstrasse 3, D-70569 Stuttgart, Germany. [2]European Synchrotron Radiation Facility, Boîte Postale 220, F-38043 Grenoble, France. [3]Abteilung Elektrochemie, Universität Ulm, Albert-Einstein-Allee 47, D-89081 Ulm, Germany.

structure, composition and defects of the passivation layer is thus needed to understand the formation of the nanopores.

The *in situ* X-ray diffraction experiments on the Cu_3Au (111) surface have been performed in the potential regime of the initial Cu dissolution shown as the bold red line in Fig. 1a. The use of a single crystal enables us to observe with high resolution the initial dealloying process as it occurs on a crystalline grain of the associated polycrystalline electrode. By recording the intensity along the momentum transfer $q_\parallel$ in the surface plane, information on the in-plane orientation and lattice parameters of epitaxial overlayers is obtained. By varying $q_\perp$ (normal to the surface, 'rod scans') the full three-dimensional structure of the overlayer is derived[20] (displayed in Fig. 1b). We note that the (111) planes exhibit the average Cu_3Au composition, and thus the corrosion process described below should be independent of ordering and disordering phenomena in the alloy.

First, we exposed the pristine surface to the de-aerated 0.1 M H_2SO_4 electrolyte with the sample potential kept at −100 mV below the equilibrium potential for Cu dissolution[21]. After this initial exposure to the electrolyte, the in-plane scan along the (1,−1,0) direction exhibits only the (2,−2,0) bulk diffraction peak from the Cu_3Au substrate. When increasing the potential up to 300 mV, a new diffraction peak can be observed at $q_\parallel$ values smaller than for the Cu_3Au (2,−2,0) diffraction peak (Fig. 2a). This new peak arises from a well-ordered, nanosized epitaxial film with an in-plane nearest-neighbour distance of $a = 280.6$ pm, which lies between that of the Cu_3Au substrate ($a = 265.2$ pm) and that of pure Au ($a = 288.4$ pm). Upon further increase of the potential, the growing peak intensity directly shows the lateral growth of the passivation layer. The observed peak shift towards the Au (2,−2,0) reflection reveals a simultaneous increase of the in-plane nearest-neighbour distance (the same behaviour was observed in all symmetry-equivalent directions). From the peak width a lateral domain size of about 20 nm is estimated. The in-plane orientational disorder of the film is typically ±1°.

The three-dimensional structure of the passivation layer is obtained from a reciprocal space map in the (1,1,−2)/(1,1,1) plane (Fig. 2b). The broad diffraction features that arise between the Cu_3Au substrate peaks give direct information on the close-packed layer stacking and orientation of the passivation layer. From the peak width a thickness of three monolayers can be estimated. The $q_\perp$ positions of the overlayer intensity distribution with respect to the substrate Bragg reflections disclose an unexpected structural feature, a CBA stacking, which inverts the ABC stacking sequence of the Cu_3Au face-centred-cubic (f.c.c.)-substrate (we note that the peak positions of the overlayer are shifted in $q_\perp$ by (1/3)·(1,1,1)). A possible explanation for this unexpected stacking inversion is the blocking of regular f.c.c. sites by adsorbates from the electrolyte.

At a potential of 270 mV, the crystallographic structure of the epitaxial layer has been determined by a quantitative measurement of the integrated intensities of several Bragg diffraction rods normal to the surface. Figure 2c shows a rod together with the best fit (red curve), obtained from a simultaneous fit of three symmetry-inequivalent rods. The structural model derived from the fit is depicted in Fig. 1b: the film consists of three hexagonally close-packed Au-enriched planes, with an inverted f.c.c. CBA stacking. The film is single-crystalline and, furthermore, does not show lateral coexistence of ABC and CBA stacked domains, which would be expected for the hetero-epitaxial growth of f.c.c. materials in the (111) direction. This implies that the stacking information from the substrate is transmitted to the film. The structural model includes two fully occupied layers, a third layer with 45% occupancy and a fourth layer with 5% occupancy. This atomic 'roughness' gives rise to a strong damping of the so-called X-ray Laue oscillations which would otherwise arise around the Bragg intensities in the direction normal to the thin film. The interlayer spacing has increased by 2% compared to the Cu_3Au bulk value of 217 pm.

For potentials between 300 mV and the critical potential at 800 mV the corrosion behaviour changes dramatically. We find that the initial passivation layer transforms into 2.6-nm-thick (12 monolayers) Au-rich islands, which inherit the inverted CBA stacking sequence. This observation can directly be inferred from the diffraction maxima along $q_\perp$ associated with the CBA stacking (Fig. 3a): the formation of Au-rich islands, which takes place after slowly increasing the potential up to 400 mV over a period of 20 h, gives rise to additional Bragg intensity, which exhibits a narrower lineshape perpendicular to the surface and a Bragg signal shifted in-plane ($q_\parallel$) towards the Au (2,−2,0) reflection (Fig. 3b). While the Bragg peak intensity of these islands grows with increasing potential, the peak intensity of the ultrathin passivation layer decreases and finally vanishes. This transition regime from the dense passivation layer to islands of the more noble component has recently been predicted by kinetic Monte Carlo simulations[22].

Ex situ atomic force microscope images of the Cu_3Au (111) surface after applying a potential >300 mV always show a surface densely covered with islands of a height >1.5 nm and 20 nm lateral dimension (Fig. 3c and d). These islands can thus be directly associated with the Au islands observed in the X-ray diffraction experiment. The Au islands exhibit a weak, but significant, short-range correlation and a homogeneous distribution of island sizes and distances that could be reminiscent of a spinodal decomposition process during island formation.

To get access to the copper concentration in the ultrathin passivation layer and in the Au islands, energy-dependent Bragg diffraction has been performed in the energy range of the Cu absorption K edge (8.979 keV). In Fig. 4 this anomalous Bragg intensity associated with the ultrathin passivation layer and the Au islands is plotted together with model calculations. For the ultrathin passivation layer a dip is observed at the position of the Cu K edge, and from the model calculation a copper concentration of 40 ± 10% can be determined. The anomalous diffraction peaks from the thicker islands exhibit no such dip and thus appear to be almost pure Au, in agreement with the observed shift of the island in-plane lattice constant towards the bulk Au value. A small deviation from the exact lattice constant of pure Au indicates that some residual strain is present and that small amounts of Cu may still be present in the islands formed at potentials above 300 mV.

This combined structural and chemical *in situ* analysis of the growth of ultrathin passivation layers allows us to understand the initial electrochemical corrosion of alloys on a microscopic level. At potentials up to 300 mV, the initial Cu dissolution leads to an ultrathin, single-crystalline f.c.c. Au-Cu alloy layer, which acts as a nanosized protection layer against further dealloying. At potentials above 300 mV, almost pure Au islands start to grow, at the expense of the initial Au-Cu alloy layer, maintaining the original, inverted CBA stacking sequence of the Au-Cu layer.

METHODS

Sample preparation. The Cu_3Au single crystal was grown in the Czochralski apparatus of the crystal growth facility of the Max-Planck-Institut für Metallforschung (MPI-MF). After mechanical polishing, the sample surface was treated by several sputter-annealing cycles under ultrahigh vacuum conditions and the surface cleanliness and the $L1_2$ superstructure ordering was verified with Auger electron spectroscopy and low-energy electron diffraction. To obtain a well-ordered superstructure, the sample was kept at a temperature 30 K below the order–disorder phase transition temperature of Cu_3Au for typically 12 h. The high quality of the surface superstructure was confirmed by surface X-ray diffraction[11]. Because the corrosion of the sample surface is an irreversible process, this preparation was repeated for each experiment. After ultrahigh-vacuum preparation and characterization, the sample was transferred in air into the electrochemical cell for the *in situ* X-ray investigation.

Electrochemical cell for *in-situ* X-ray diffraction. Besides the Cu_3Au working electrode, the cell is equipped with a Pt counter electrode and a Ag/AgCl miniature reference electrode. It is sealed with a 6-μm-thick Mylar foil, allowing entrance and exit of the X-ray beam[11,23]. For the measurements of diffracted intensities the Mylar foil was slightly pressed on the sample surface by applying an under-inflation to the electrolyte in the cell. In this way the absorption of X-ray intensity can be minimized, despite a grazing incidence angle of less than 1°, while leaving a micrometre-thick layer of electrolyte above the surface and thus keeping the surface immersed and under potential control. Before changing the electrode potential, the electrolyte pressure was increased, providing a several-millimetre-thick solution layer above the sample surface.

X-ray diffraction. Cu_3Au is an ordered alloy in the cubic f.c.c.-like $L1_2$ structure ($a_0 = 375$ pm). All measurements are expressed in bulk reciprocal lattice coordinates of the Cu_3Au substrate. The surface X-ray diffraction measurements were carried out using z-axis and 2 + 2 diffractometers equipped with point detectors at beamline ID32 at the European Synchrotron Radiation Facility (ESRF) and the beamline BW2 at the Hamburger Synchrotronstrahlungslabour (HASYLAB at DESY). The measurements were performed with an incident angle close to the critical angle for total external reflection of Cu_3Au. Integrated intensities were obtained from rocking scans around the sample surface normal, after background subtraction and application of standard correction factors. The fitting of the integrated intensities was performed using the software package ROD[20]. In anomalous diffraction experiments we make use of the fact that the dispersion correction f' to the atomic form factor f gets negative close to an X-ray absorption edge, which can significantly reduce the real part of f: $\mathrm{Re}(f) = f_0 + f'$. The measurements were corrected for the energy dependence of the optical transmission function of the sample and for the energy-dependent absorption of the Mylar foil and the electrolyte.

Received 30 April; accepted 10 November 2005.

1. Koch, G. H., Brongers, M. P. H., Thompson, N. G., Virmani, Y. P. & Payer, J. H. *Corrosion Cost and Preventive Strategies in the United States*. Report

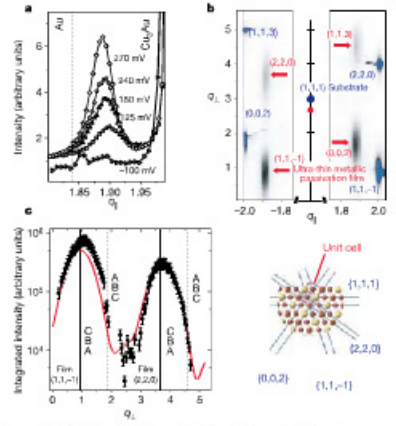

Figure 2 | *In-situ* structural characterization of the passivation layer. **a**, Diffracted intensity along $q_\parallel$ in units of (1, −1,0) for varying electrochemical potential; the statistical error bar is below the symbol size. A Bragg peak from the epitaxial passivation layer is growing at (1.89,−1.89,0); in addition the (2,−2,0) substrate peak is observed. **b**, Experimental reciprocal space map in the (1,1,−2)/(1,1,1) plane characteristic for the potential regime from −100 mV to 270 mV. $q_\parallel$ is given in units of 1/3(1,1,−2). The Bragg reflections from the passivation layer and the Cu_3Au substrate are observed and from the shift of the Bragg peak positions between the substrate and the film along $q_\perp$, it can be inferred that an epitaxial, single-crystalline overlayer with inverted CBA stacking is forming. **c**, Integrated intensities of the ultrathin passivation layer along $q_\perp$ ($q_\parallel = (1.89,-1.89,0)$); the red line represents the best fit to the data based on the structural model depicted in Fig. 1b. Solid lines indicate the $q_\perp$ position for a layer with CBA stacking, dashed lines the $q_\perp$ position for an ABC stacking.

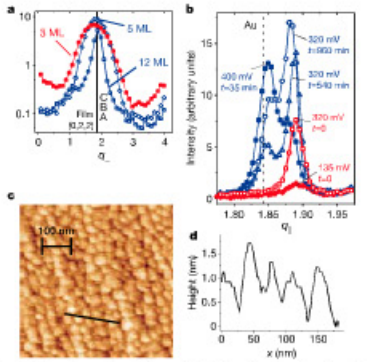

Figure 3 | Transformation of the passivation layer into Au islands. **a**, The ultrathin layer gives rise to a broad intensity distribution along $q_\perp$. With both in-plane peaks present, the pure gold peak in the corresponding $q_\perp$-scan has a much narrower width, indicating an island height of typically 10–15 monolayers (2–3 nm). The ultrathin passivation layer is transforming into Au islands, maintaining predominantly the initial CBA stacking. **b**, By increasing the potential above 300 mV on the timescale of hours, an in-plane peak at a $q_\parallel$ position close to epitaxial gold is emerging in addition to the ultrathin passivation layer peak. **c**, *Ex situ* atomic force microscope image (0.5 μm × 0.5 μm) after applying a potential of 450 mV versus Ag/AgCl: in this potential regime the formation of 2–3-nm-thick pure Au islands was observed in the X-ray diffraction experiments, which is a typical corrugation of the surface. **d**, Height along the line segment in **c**. The typical lateral dimension of the islands is 20 nm. The measured vertical corrugation of 1.5 nm is probably limited by tip effects.

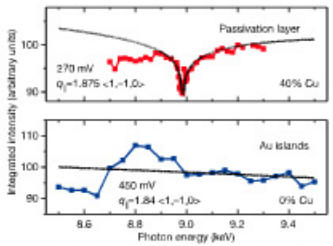

Figure 4 | Integrated anomalous in-plane diffraction intensities of the ultrathin passivation layer, and Au islands. The solid lines represent model calculations with varying Cu concentration. For the diffraction intensity of the passivation layer (top) a dip at the copper K edge is clearly visible owing to the contribution of the anomalous dispersion f' and absorption f'' correction factors to the atomic form factor of Cu, and the model calculations agree best for a Cu concentration of 40%. The signal from the Au islands (bottom) exhibits no contribution of copper to the diffracted intensity.

FHWA-RD-01-156 (Report by CC Technologies Laboratories, Inc. to Federal Highway Administration (FHWA), Office of Infrastructure Research and Development, McLean, 2001); (http://www.corrosioncost.com/pdf/main.pdf).
2. Erlebacher, J., Aziz, M. J., Karma, A., Dimitrov, M. & Sieradzki, K. Evolution of nanoporosity in dealloying. *Nature* **410**, 450–453 (2001).
3. Weissmüller, J. *et al.* Charge-induced reversible strain in a metal. *Science* **300**, 312–315 (2003).
4. Al-Kharafi, F. M., Ateya, B. G. & Allah, R. M. Selective solution of brass in salt water. *Appl. Electrochem.* **34**, 47–53 (2004).
5. Williams, D. E., Newman, R. C., Song, Q. & Kelly, R. G. Passivity breakdown and pitting corrosion of binary alloys. *Nature* **350**, 216–219 (1991).
6. Gerischer, H. in *Corrosion* Vol. 14 (ed. Heumann, T.) 59–64 (Chemie, Weinheim, 1962).
7. Pickering, H. W. Characteristic features of alloy polarization curves. *Corr. Sci.* **23**, 1107–1120 (1983).
8. Kaiser, H. & Eckstein, G. A. in *Corrosion of Alloys—Encyclopedia of Electrochemistry* (eds Stratmann, M. & Frankel, G. S.) Vol. 4, 156–186 (Wiley, Weinheim, 2003).
9. Oppenheim, I. C., Trevor, D. J., Chidsey, Ch. E. D., Trevor, P. L. & Sieradzki, K. In-situ scanning tunnelling microscopy of corrosion of silver-gold alloys. *Science* **254**, 687–689 (1991).
10. Chen, S. J. *et al.* Selective dissolution of copper from Au-rich Cu-Au alloys: an electrochemical study. *Surf. Sci.* **292**, 289–297 (1993).
11. Eckstein, G. A. *In-situ Rastertunnelmikroskopische Untersuchungen zur selektiven Korrosion von niedrigindizierten $Au_xCu(h0l)$ und $Cu_xAu(h0l)$ Legierungseinkristallen*. Dissertation, Erlangen (2001).
12. Stratmann, M. & Rohwerder, M. A pore view of corrosion. *Nature* **410**, 420–423 (2001).
13. Moffat, T. P., Fan, F.-R. F. & Bard, A. J. Electrochemical and scanning tunneling microscopic study of dealloying of Cu_3Au. *J. Electrochem. Soc.* **138**, 3224–3235 (1991).
14. Kabius, B., Kaiser, H. & Kaesche, H. in *Surfaces Inhibition and Passivation* (eds McCafferty, E. & Brodd, R. J.) 562–573 (The Electrochemical Society, Pennington, 1986).
15. Li, R. & Sieradzki, K. Ductile-brittle transition in random porous Au. *Phys. Rev. Lett.* **68**, 1168–1171 (1992).
16. Pickering, H. W. & Swann, P. R. Electron metallography of chemical attack upon some alloys susceptible to stress corrosion cracking. *Corrosion* **19**, 373t–389t (1963).
17. Forty, A. J. Corrosion micromorphology of noble metal alloys and depletion gilding. *Nature* **282**, 597–598 (1979).
18. Forty, A. J. & Rowlands, G. A. Possible model for corrosion pitting and tunnelling in noble metal alloys. *Phil. Mag. A* **43**, 171–188 (1980).
19. Pickering, H. W. Formation of new phases during anodic dissolution of Zn-rich Cu-Zn alloys. *J. Electrochem. Soc.* **117**, 8–15 (1970).
20. Robinson, I. K. & Tweet, D. J. Surface X-ray diffraction. *Rep. Prog. Phys.* **55**, 599–651 (1992).
21. Zoubov, N., Vanleugenhage, C. & Pourbaix, M. in *Atlas d'Equilibres Electrochemique* (ed. Pourbaix, M.) Ch. 14 (Gauthier Villars, Paris, 1963).
22. Erlebacher, J. An atomistic description of dealloying. *J. Electrochem. Soc.* **151**, C614–C626 (2004).
23. Stierle, A. *et al.* Dedicated Max-Planck beamline for the in-situ investigation of interfaces and thin films. *Rev. Sci. Instrum.* **75**, 5302–5307 (2004).
24. Fleischmann, M. & Mao, B. W. In-situ X-ray diffraction studies of Pt electrode/solution interfaces. *J. Electroanal. Chem.* **229**, 125–139 (1987).
25. Zegenhagen, J. *et al.* X-ray diffraction study of a semiconductor/electrolyte interface: n-GaAs(001)/H_2SO_4/(Cu). *Surf. Sci.* **352–354**, 346–351 (1996).
26. Vlieg, E. ROD: a program for surface X-ray crystallography. *J. Appl. Crystallogr.* **33**, 401–405 (2000).

Acknowledgements We thank B. Krause, A. Reichn, S. Warren, B. C. C. Cowie, S. Thiess, O. Bunk and W. Drube for their help with the synchrotron measurements, and F. D'Anca and R. Felici for collaboration in developing the *in-situ* cell and installing the electrochemistry laboratory at INFM-OGG/ESRF. The Bundesministerium für Forschung und Bildung (BMBF) is acknowledged for financial support.

LETTERS

Winter forest soil respiration controlled by climate and microbial community composition

Russell K. Monson[1,2]*, David L. Lipson[4]*, Sean P. Burns[1,5], Andrew A. Turnipseed[5], Anthony C. Delany[5], Mark W. Williams[3] & Steven K. Schmidt[1]

Most terrestrial carbon sequestration at mid-latitudes in the Northern Hemisphere occurs in seasonal, montane forest ecosystems[1]. Winter respiratory carbon dioxide losses from these ecosystems are high, and over half of the carbon assimilated by photosynthesis in the summer can be lost the following winter[2,3]. The amount of winter carbon dioxide loss is potentially susceptible to changes in the depth of the snowpack; a shallower snowpack has less insulation potential, causing colder soil temperatures and potentially lower soil respiration rates. Recent climate analyses have shown widespread declines in the winter snowpack of mountain ecosystems in the western USA and Europe that are coupled to positive temperature anomalies[4–6]. Here we study the effect of changes in snow cover on soil carbon cycling within the context of natural climate variation. We use a six-year record of net ecosystem carbon dioxide exchange in a subalpine forest to show that years with a reduced winter snowpack are accompanied by significantly lower rates of soil respiration. Furthermore, we show that the cause of the high sensitivity of soil respiration rate to changes in snow depth is a unique soil microbial community that exhibits exponential growth and high rates of substrate utilization at the cold temperatures that exist beneath the snow. Our observations suggest that a warmer climate may change soil carbon sequestration rates in forest ecosystems owing to changes in the depth of the insulating snow cover.

The recent global proliferation of tower-measurement networks has made it possible to analyse details of the coupling between climate dynamics and the carbon (*C*) cycle[7]. Most past studies have focused on ecosystem–atmosphere CO_2 exchange during the growing season because the instantaneous flux rates are so much higher than during colder periods. In seasonal forests, however, small but continuous rates of ecosystem respiration during the winter can, in some cases, completely determine annual rates of C sequestration[2,3]. Studies using artificial snow removal have demonstrated a critical role for thermal insulation in determining winter biogeochemical cycling[8–10]. In this study, we aimed to move beyond experimental manipulations of snow cover, which can cause artificial treatment effects, and examine the factors that control winter soil C cycling within the context of natural climate variation.

We used the eddy covariance approach between 1 November 1998 and 31 October 2004 to continuously measure net ecosystem CO_2 exchange (NEE) at the Niwot Ridge Ameriflux site in the Rocky Mountains. Interannual variation in late-winter (1 March–15 April) cumulative NEE was not correlated with variation in mean air temperature ($P < 0.05$, Fig. 1a), but was correlated with variation in mean soil temperature (Fig. 1b) which, in turn, was correlated with variation in the 1 April snow-water equivalent (SWE), a measure of the cumulative winter snow pack (Fig. 1c). The relationship between mean soil temperature and SWE is best explained by a second-order polynomial, reflecting an asymptote at high snow depths as soil temperature approached its natural limit of 0 °C. The mean 1 April SWE for the period 1982–2004 at the Niwot Ridge site is 36.7 ± 3.3 cm, which falls just above the threshold of 31.4 cm, below which decreases in SWE affect late-winter NEE; nine of the past 23 years (39%) have been characterized by 1 April SWE values that fall below this threshold.

We developed a first-order exponential coefficient (R_T) to describe the temperature sensitivity of respiration (analogous to the Q_{10} coefficient used in biochemical studies). The interannual temperature dependency described by R_T was 6.6 when determined across all six years (Fig. 1b). The interannual range in late-winter NEE

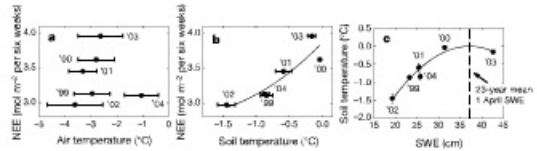

Figure 1 | Responses of NEE to air and soil temperature as influenced by SWE for the indicated years. a, The response of NEE to average daily air temperature. **b**, The response of NEE to average daily soil temperature ($y = ae^{xp^{bx}}$, $a = 3.8244$, $b = 0.1963$, $R^2 = 0.81$, $P = 0.0152$). **c**, The relationship between SWE (on 1 April) and average daily soil temperature ($y = ax^2 + bx + c$, $a = -0.0046$, $b = 0.339$, $c = -6.320$, $R^2 = 0.944$, $P = 0.0129$). Error bars are mean ± s.e. Data are for 1 March to 15 April.

[1]Department of Ecology and Evolutionary Biology, [2]Center for Interdisciplinary Research in Environmental Science, [3]Department of Geography and Institute of Arctic and Alpine Research, University of Colorado, Boulder, Colorado 80309, USA. [4]Department of Biology, San Diego State University, San Diego, California 92182, USA. [5]National Center for Atmospheric Research, PO Box 3000, Boulder, Colorado 80305, USA.
*These authors contributed equally to this work.